J. Fluid Mech. (2022), *vol*. 944, A47, doi:10.1017/jfm.2022.513

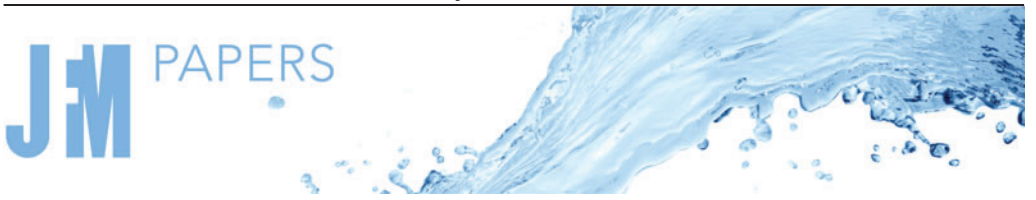

Wavenumber lock-in and spatial parametric resonance in convection

M.Z. Hossain[1],† **and J.M. Floryan**[1]

[1]Department of Mechanical and Materials Engineering, The University of Western Ontario, London, ON N6A 5B9, Canada

(Received 17 September 2021; revised 25 May 2022; accepted 3 June 2022)

Analysis of convection driven by spatial periodic heating shows a wealth of responses due to Prandtl number dependence. The primary convection is delineated by the heating wavenumber and the secondary convection is characterized by the critical wavenumber established by an instability process. The resulting two-wavenumber dynamical system involves spatial parametric resonance leading to the wavenumber lock-in and the Rayleigh–Bénard (RB) instability producing unlocked states. Heating conditions leading to the co-existence of both types of states have been identified. Transition from the locked to the unlocked states produces states with a wide range of wavelengths and diverse patterns of movement. The possible secondary states are driven by a competition between the RB mechanism and the spatial parametric resonance. The relative strengths of these mechanisms change with Prandtl number Pr resulting in four types of system responses. In the type A response occurring for $Pr > 0.4$, parametric resonance dominates for the heating wavenumber $\alpha < 4.5$ resulting in the pattern lock-in between the primary and secondary convections whereas RB occurs for $\alpha > 10$. There is a wealth of possible convection patterns in the in-between zone where a small change of α results in a major change of flow pattern. In the type B response, which occurs for $0.19 < Pr < 0.4$, the RB effect dominates eliminating the lock-in. The type C response, which occurs for $0.08 < Pr < 0.19$, is similar to type A but stronger spatial modulation extends the range of dominance of parametric resonance up to $\alpha = 7$ while the RB effect dominates for $\alpha > 10$ as in the type A response. A wealth of possible patterns occurs in the transition zone ($7 < \alpha < 10$). In the type D response, which occurs for $Pr < 0.08$, the strong spatial modulation results in the formation of two separate critical stability curves, one resulting from the dominance of the spatial parametric resonance leading to the lock-in effect, and the other one corresponding to the dominance of the RB effect producing unlocked states. No continuous transition between both states can occur. Conditions where both distinct states can arise simultaneously were identified. Morphing between different patterns of

† Email address for correspondence: mhossa7@uwo.ca

secondary convection may occur in response to small changes in the heating pattern in types A and C, while such processes are not possible in types B and D.

Key words: buoyancy-driven instability

1. Introduction

Convection driven by spatial temperature patterns exhibits properties fundamentally different from the classical Rayleigh–Bénard (RB) instability (Bénard 1900; Rayleigh 1916), as the latter deals with uniformly heated walls and the onset of instability is independent of Prandtl number Pr (Kelly & Pal 1978; Bodenschatz, Pesch & Ahlers 2000; Krishnan, Ugaz & Burns 2002; Freund, Pesch & Zimmermann 2011), while the former deals with non-uniformly heated walls with the formation of a horizontal temperature gradient and a strong effect of Pr at the onset of instability (Lyubimov *et al.* 2009; Hossain & Floryan 2013*b*, 2014, 2015). It is known that reduction of Pr strengthens the influence of spatial modulations (Hossain & Floryan 2013*a*) but its effects on the secondary states are yet to be studied. Temperature patterns represent external forcing generating spatial modulations (primary convection) which, under certain conditions, transit to secondary states (Hossain & Floryan 2013*b*). The results in these literature are limited to a single Prandtl number ($Pr = 0.71$) for which the primary response of the system consists of stationary convection rolls with the axis orthogonal to the heating wave vector. The structure of these rolls is determined by the heating intensity, as measured by the Rayleigh number Ra, and by the heating wavenumber α. It is known that an increase of α leads to formation of a convection boundary layer near the heated wall with all spatial modulations confined to this layer. A conduction zone emerges above this layer and the fluid there sees its edge as a uniformly heated wall. Thus, the outer layer can be considered as a layer subject to RB instability.

Transition to the secondary states is driven by a competition between the spatial parametric resonance (Manor, Hagberg & Meron 2008, 2009) and the RB mechanism (Bénard 1900; Rayleigh 1916). The former one produces the locked-in states where the primary rolls have a sub-harmonic relation with the secondary structures, and the latter one produces states well described in the literature. A transition zone where neither of these mechanisms dominates leads to the formation of a range of commensurate states with widely different properties and appearance of soliton matrices (Lowe & Gollub 1985; Hossain & Floryan 2013*b*), as well as system frustration as multiple states of the system are possible (Nixon *et al.* 2013). Many of the possible states cannot be predicted by the Bloch theory for periodic systems (Bloch 1928; Floryan & Inasawa 2021).

This analysis is focused in the first step on the identification of the primary system response to variations of Pr in the range from 10^{-2} to 10^{3} which covers values of Pr which are of practical importance (Verzicco & Camussi 1999; Lyubimov *et al.* 2009). It explores in the second step transition to secondary states, how the relative strengths of two instability mechanisms is affected by variations of Pr and what its consequences are. In particular, we investigate how parametric resonance changes with Pr and what is the range of α producing locked-in states. We investigate how the range of α where the RB mechanism dominates changes with Pr. Finally we explore the system responses for the range of α where both mechanisms are in balance, how the system responses change with Pr and how various commensurate states are formed. Section 2 discusses the primary convection which represents the forced response of the fluid. Section 3 discusses transition

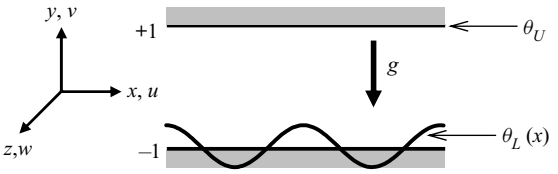

Figure 1. Sketch of the flow configuration.

to secondary states and various topologies emerging from the system bifurcation. Section 4 provides a summary of the main findings.

2. Primary convection

The analysis is carried out using a model problem, as shown in figure 1, consisting of a horizontal slot between two parallel walls extending to $\pm\infty$ in the x-direction filled in with a Boussinesq fluid (Koschmieder 1993) and exposed to spatial periodic heating at the lower wall while keeping the upper wall isothermal. The lower (θ_L) and upper (θ_U) walls' temperatures are

$$\theta_L(x) = \tfrac{1}{2}\cos(\alpha x), \quad \theta_U(x) = 0, \tag{2.1}$$

where α stands for the heating wavenumber, θ denotes the relative temperature, i.e. $\theta = T - T_{ref}$, T denotes the temperature and T_{ref} stands for the upper wall (reference) temperature. The fluid has thermal conductivity k, specific heat per unit mass c, thermal diffusivity $\kappa = k/\rho c$, kinematic viscosity ν, dynamic viscosity μ, thermal expansion coefficient Γ and density ρ. Horizontal temperature gradients drive convective rolls. The resulting temperature field is split into conductive (θ_c) and convective (θ_1) components, i.e.

$$\theta(x, y) = Pr^{-1}\theta_c(x, y) + \theta_1(x, y), \tag{2.2}$$

$$\theta_c(x, y) = \frac{1}{4}\left[\frac{\cosh(\alpha y)}{\cosh(\alpha)} - \frac{\sinh(\alpha y)}{\sinh(\alpha)}\right]\mathrm{e}^{\mathrm{i}\alpha x} + \text{c.c.}, \tag{2.3}$$

where c.c. stands for the complex conjugate. The amplitude of temperature variations along the wall T_d is used as the conductive scale and $T_v = T_d\nu/\kappa$ as the convective scale – $T_v/T_d = Pr$ with $Pr = \nu/\kappa$. The half-distance h between the walls is used as the length scale, $U_v\nu/h$ as the (convective) velocity scale and $P_v = \rho U_v^2$ as the pressure scale. The convective component is described by

$$\frac{\partial u_1}{\partial x} + \frac{\partial v_1}{\partial y} = 0, \tag{2.4a}$$

$$u_1\frac{\partial u_1}{\partial x} + v_1\frac{\partial u_1}{\partial y} = -\frac{\partial p_1}{\partial x} + \nabla^2 u_1, \tag{2.4b}$$

$$u_1\frac{\partial v_1}{\partial x} + v_1\frac{\partial v_1}{\partial y} = -\frac{\partial p_1}{\partial y} + \nabla^2 v_1 + Ra\theta_1 + RaPr^{-1}\theta_c, \tag{2.4c}$$

$$Pr\left(u_1\frac{\partial \theta_1}{\partial x} + v_1\frac{\partial \theta_1}{\partial y}\right) + u_1\frac{\partial \theta_c}{\partial x} + v_1\frac{\partial \theta_c}{\partial y} = \nabla^2\theta_1, \tag{2.4d}$$

$$u_1(\pm 1) = 0, \quad v_1(\pm 1) = 0, \quad \theta_1(\pm 1) = 0. \tag{2.4e–g}$$

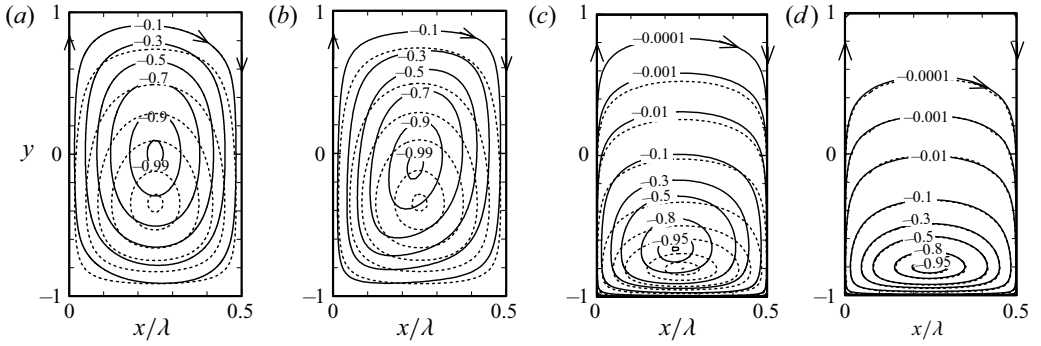

Figure 2. Flow topologies for $\alpha = 3$ (*a*,*b*) and $\alpha = 10$ (*c*,*d*) for $Ra = 1$ (dotted lines) and $Ra = 10^4$ (solid lines). Plots (*a*,*c*) and (*b*,*d*) correspond to $Pr = 0.01$, 1000, respectively. Streamfunction is normalized with its maximum $\psi_{1,max}$. In plots (*a–d*): $\psi_{1,max} = (0.128, 580.1)$, $(1.22 \times 10^{-6}, 7.3 \times 10^{-3})$, $(3.38 \times 10^{-3}, 26.37)$, $(3.38 \times 10^{-8}, 3.32 \times 10^{-4})$ for $Ra = 1, 10^4$.

In the above $\boldsymbol{v}_1 = (u_1, v_1)$ denotes the velocity vector, p_1 stands for the pressure, $Ra = g\Gamma h^3 T_d/\nu\kappa$ is the (periodic) Rayleigh number, ∇^2 denotes the Laplace operator and dissipation effects have been neglected. The last term on the right-hand side of (2.4*c*) provides spatial modulation which is inversely proportional to Pr – an increase of Pr significantly diminishes this modulation. Therefore, the strength of the rolls is expected to increase with a reduction of Pr and decrease with an increase of Pr. The above system was solved with spectral accuracy using the method described in Hossain & Floryan (2013*a*) and discussed in Appendix A.

The primary convection driven directly by periodic heating represents a forced response. This response establishes a spatially modulated flow field and transition of this field to secondary states, which is of interest – Pr determines the strength of this modulation and leads to widely different system responses.

2.1. *Description of the primary convection*

This section provides a description of the primary convection and how it changes as a function of fluid thermal properties expressed by the Prandtl number Pr. Various flow features are captured using the streamfunction ψ_1 defined in the usual manner as $u_1 = \partial\psi_1/\partial y$, $v_1 = -\partial\psi_1/\partial x$, which together with the convective temperature field θ_1 are expressed using the following Fourier representation:

$$[\psi_1, \theta_1](x, y) = \sum_{n=-\infty}^{n=+\infty} [\varphi_1^{(n)}, \phi_1^{(n)}] \mathrm{e}^{\mathrm{i}n\alpha x}. \tag{2.5}$$

Here, $\varphi_1^n = \varphi_1^{(-n)*}$ and $\phi_1^n = \phi_1^{(-n)*}$ represent the reality conditions and stars denote complex conjugates.

Convective motion has a simple topology that changes marginally with variations of Pr, as illustrated in figure 2. The fluid rises above the hot spots and descends above the cold spots forming closed, counter-rotating rolls. An increase of Ra results in centres of these rolls moving upwards and towards the hot spots. The fluid movement concentrates closer to the lower wall as α increases. An increase of Pr produces a similar effect.

Results displayed in figure 3(*a*) demonstrate that the strength of the rolls, as measured by the maximum of the streamfunction ψ_{max}, increases proportionally to Ra regardless of

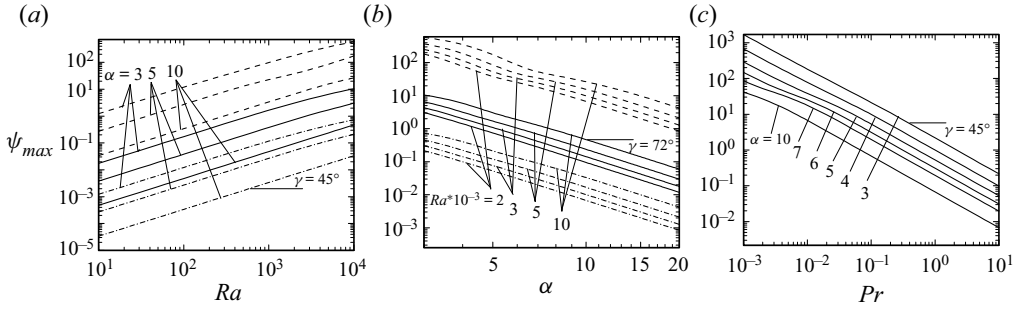

Figure 3. Variations of the roll strength (as measured by the maximum of the streamfunction $\psi_{1,max}$ denoted as ψ_{max}) as a function of Ra (a), as a function of α (b) and as a function of Pr (c). Dashed, continuous and dash-dotted lines correspond in plots (a,b) to $Pr = 0.01, 0.71, 10$, respectively.

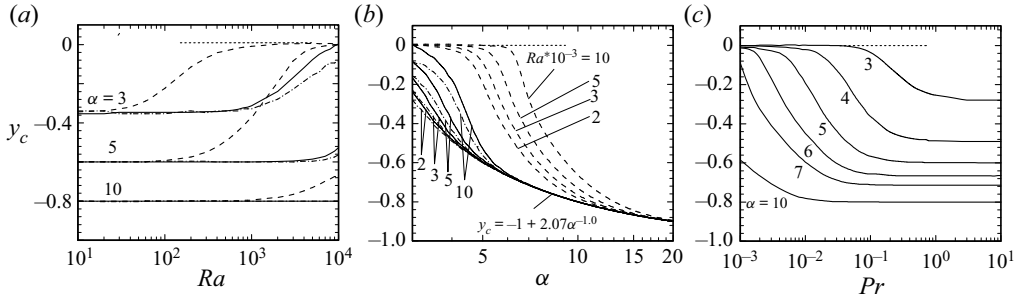

Figure 4. Variations of the location of the roll centre y_c as a function of Ra (a), as a function of α (b) and as a function of Pr (c). Dashed, continuous and dash-dotted lines correspond in plots (a,b) to $Pr = 0.01, 0.71, 10$, respectively. Data for the last two values of Pr overlap in plot (a).

the type of fluid – this intensity is much higher for smaller Pr values. Results displayed in figure 3(b) demonstrate that the strength of convection decreases proportionally to α^{-3} for all Ra and Pr values of interest, with convection for the lowest Pr values being the strongest. Results displayed in figure 3(c) demonstrate that the strength of convection decreases proportionally to Pr.

Results displayed in figure 4 provide information about adjustments of flow topology due to variations of Pr. While this topology remains qualitatively similar, the subtle variations can be measured using the position of the roll centre y_c and thickness h_v of the convection boundary layer forming near the heated wall. This thickness is determined by comparing the heat flow carried by mode zero from the temperature field representation with the heat flow carried by the remaining modes. Use of only the first three temperature modes from (2.5) provided sufficient accuracy for evaluation of h_v. Quantity E defined below expresses the ratio of both heat flows, i.e.

$$E = ([(\alpha\phi_1^{(1)})^2 + (2\alpha\phi_1^{(2)})^2]^{1/2} + [(D\phi_1^{(1)})^2 + (D\phi_1^{(2)})^2]^{1/2})/|D\phi_1^{(0)}|, \tag{2.6}$$

with $D = \mathrm{d}/\mathrm{d}y$, and the location where $E = 0.05$ was used to define the edge of the convection boundary layer – this criterion was rather arbitrary but well illustrates evolution of the structure of the temperature field.

Results displayed in figure 4(a) demonstrate that the position of the roll centre remains constant for low Ra values but, once a certain critical Ra is reached, the centre starts moving upwards and reaches the centre of the slot for high enough Ra values. An increase

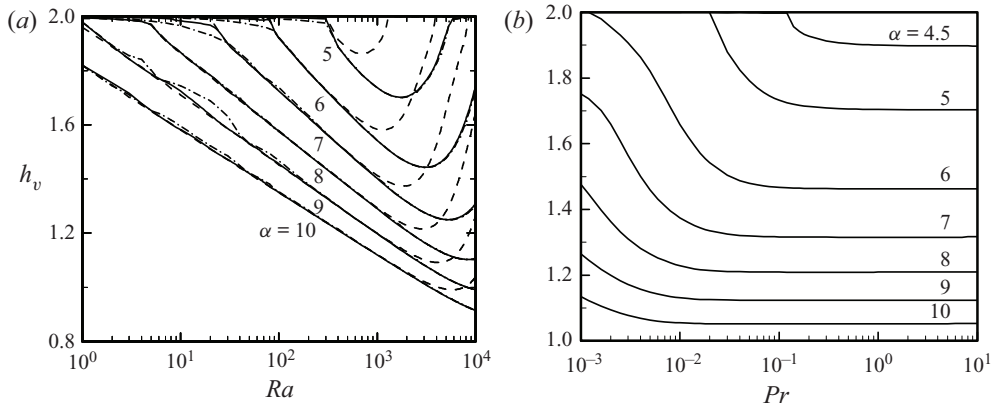

Figure 5. Variations of the thickness h_v of the convection boundary layer as a function of α and Ra for $Pr = 0.01$, 10 (a), and as a function of Pr and α for $Ra = 2000$ (b). Dashed and continuous lines correspond in plot (a) to $Pr = 0.01$, 10, respectively.

of α causes this transition to take place at higher Ra values. The effects of α are captured explicitly in figure 4(b). The roll centre moves downwards with an increase of α and its locations follow an asymptote in the form $y_c = -1 + 2.07\alpha^{-1}$ for large enough values of α for all Ra and Pr values considered. The approach to the asymptote is slowest for the smallest Pr values. The effects of Pr are captured explicitly in figure 4(c). Roll centres are located in the middle of the slot for small enough Pr values and move to a new, Pr-independent location for high enough Pr values. This new location is a function of α – the transition between the two limiting positions occurs for Pr between ~ 0.01 and ~ 0.2.

Variations of the thickness h_v of the convective boundary layer (distance from the lower wall till the edge of the boundary layer) as a function of Ra are illustrated in figure 5(a). It can be seen that the convection occurs in the whole interior of the slot for $\alpha < 5$ for low Pr fluids (e.g. $Pr = 0.01$) with this range decreasing to $\alpha <\sim 4.5$ for large Pr fluids (e.g. $Pr = 10$). An increase of α beyond these limits confines convection to a boundary layer near the heated wall whose thickness decreases as α increases. A distinct conduction layer forms above the boundary layer but only for a finite range of Ra. For example, a distinct conduction layer is formed for $Pr = 0.01$ and $\alpha = 5$ for Ra between 300 and 1200. The range of Ra expands towards smaller and larger values as α increases. For $\alpha = 10$, this range extends from $Ra < 1$ on the low end till $Ra > 10^4$ on the large end. The character of the curves suggests that the conductive zone will disappear if Ra becomes sufficiently large even for large values of α, e.g. $\alpha = 10$. Figure 5(b) illustrates the effects of variations of Pr on the thickness of the boundary layer h_v for $Ra = 2000$. Variations of Pr cease to affect thickness for $Pr >\sim 0.2$ regardless of α. Major changes of the thickness occur for $Pr <\sim 0.2$ and these changes are more pronounced at smaller values of α.

The above discussion shows that topology of the flow field is qualitatively similar for all Pr values, but its quantitative properties change significantly with an increase of intensity of convection caused by a decrease of Pr and an earlier formation of the convective boundary layer with an increase of Pr. We shall discuss in the next section how these changes affect the onset and form of secondary convection.

3. Secondary convection

The onset and form of secondary states are established using the linear stability theory (Floryan 1997; Hossain & Floryan 2013*b*). We superimpose unsteady, two-dimensional infinitesimal disturbances into the primary convection and the resulting flow fields are represented as

$$\boldsymbol{v} = \boldsymbol{v_1}(x, y) + \boldsymbol{v_2}(x, y, t), \quad \theta = Pr^{-1}\theta_c(x, y) + \theta_1(x, y) + \theta_2(x, y, t), \quad p = p_1(x, y) + p_2(x, y, t). \tag{3.1a–c}$$

In the above the subscript 2 refers to the disturbance fields, $\boldsymbol{v_2} = (u_2, v_2)$ stands for the disturbance velocity vector, θ_2 denotes the temperature disturbance and $p_2(x, y, t)$ stands for the disturbance pressure field. The assumed form (3.1) of the flow quantities is substituted into the field equations, the base part (the primary convection, (2.4)) is subtracted and the equations are linearized. The resulting disturbance equations have the form

$$\frac{\partial u_2}{\partial x} + \frac{\partial v_2}{\partial y} = 0, \tag{3.2a}$$

$$\frac{\partial u_2}{\partial t} + u_1\frac{\partial u_2}{\partial x} + u_2\frac{\partial u_1}{\partial x} + v_1\frac{\partial u_2}{\partial y} + v_2\frac{\partial u_1}{\partial y} = -\frac{\partial p_2}{\partial x} + \nabla^2 u_2, \tag{3.2b}$$

$$\frac{\partial v_2}{\partial t} + u_1\frac{\partial v_2}{\partial x} + u_2\frac{\partial v_1}{\partial x} + v_1\frac{\partial v_2}{\partial y} + v_2\frac{\partial v_1}{\partial y} = -\frac{\partial p_2}{\partial y} + \nabla^2 v_2 + Ra\theta_2, \tag{3.2c}$$

$$Pr\left(\frac{\partial \theta_2}{\partial t} + u_1\frac{\partial \theta_2}{\partial x} + u_2\frac{\partial}{\partial x}\left(\frac{\theta_c}{Pr} + \theta_1\right) + v_1\frac{\partial \theta_2}{\partial y} + v_2\frac{\partial}{\partial y}\left(\frac{\theta_c}{Pr} + \theta_1\right)\right) = \nabla^2\theta_2, \tag{3.2d}$$

$$u_2(\pm 1) = 0, \quad v_2(\pm 1) = 0, \quad \theta_2(\pm 1) = 0. \tag{3.2e–g}$$

The disturbance quantities are represented as

$$[\boldsymbol{v_2}, \theta_2, p_2](x, y, t) = [\boldsymbol{V_2}, \Theta_2, P_2]\,(x, y)\mathrm{e}^{\mathrm{i}(\delta x - \sigma t)} + \text{c.c.}, \tag{3.3}$$

where δ is the disturbance wavenumber, the real and imaginary parts of the complex exponent $\sigma = \sigma_r + \mathrm{i}\,\sigma_i$ describe the rate of growth and the frequency of disturbances with positive σ_i identifying instability and c.c. stands for the complex conjugate. The x-periodic amplitudes $\boldsymbol{V_2}(x, y)$, $\Theta_2(x, y)$ and $P_2(x, y)$ are defined using Floquet ansatz of the form

$$[\boldsymbol{V_2}, \Theta_2, P_2](x, y) = \sum_{m=-\infty}^{m=+\infty} [\boldsymbol{V_2^{(m)}}, \Theta_2^{(m)}, P_2^{(m)}](y)\mathrm{e}^{\mathrm{i}\,m\alpha x}. \tag{3.4}$$

The linear disturbance equations represent an eigenvalue problem and relation between $\sigma, \delta, Ra, Pr, \alpha$ (the dispersion relation) that needs to be established numerically. The discretization process and the numerical solution are described in Appendix B and Hossain & Floryan (2013*b*).

The strength of the x-periodic modulation of the primary convection increases with a reduction of Pr, as discussed in the previous section, and it is expected to affect the onset of secondary convection. Various scans through the parameter space identified the presence of only stationary modes, i.e. $\sigma_r = 0$, in the range of α and Ra subject to investigations.

3.1. *Onset of the secondary convection*

The structures of the secondary convection that we shall focus on consist of rolls parallel to the primary rolls and shall be referred to as longitudinal rolls. They illustrate features of spatial parametric resonance in the most pronounced manner. The primary rolls are characterized by the heating wavenumber α and the secondary rolls are characterized by the critical disturbance wavenumber δ_{cr} – properties of the complete system depend on the ratio of these two wavenumbers which can lead either to commensurate or incommensurate states. The onset (or critical) conditions (the critical Rayleigh number Ra_{cr} and the critical disturbance wavenumber δ_{cr}) need to be established numerically for each α which means that incommensurate states cannot be accessed (due to the finite computer word length), but their existence can be deduced indirectly.

We begin the discussion of the onset of secondary states with a global look at possible system responses as provided in figure 6 displaying variations of the critical conditions as functions of Pr. The reader should recall that the onset of the RB convection does not depend on Pr (Chandrasekhar 1961), while Pr plays a major role in the onset of secondary convection considered here (figure 6). There is a well-defined large-Pr limit which is reached for $Pr > 10$ where the critical conditions, the lock-in zone (with its border defined by the lock-in wavenumber $\alpha_{lc} = 4.35$) and the minimum of $Ra_{cr} = 2890$ (at $\alpha = 3.93$) do not depend on Pr (see figure 6*a*). A decrease of Pr from 10 to 0.71 results in an increase of the smallest Ra_{cr} which subsequently decreases with a further reduction of Pr. No well-defined universal state exists for the small-Pr limit as Ra_{cr} decreases over the whole range of α subject to this investigation. The break-up of a single $Ra_{cr}(\alpha)$ branch into two distinct branches, one dominated by the spatial parametric resonance and the other dominated by the RB mechanism, is well illustrated in figure 6(*b*). The extend of the left branch increases with a reduction of Pr as stronger spatial modulations lead to a more effective parametric resonance. The form of the secondary state changes in a non-monotonic manner – the lock-in is observed in some range of α for all Pr values except for $0.19 < Pr < 0.4$ where the RB effect dominates, and for $Pr < 0.08$ where two distinct branches are formed which invalidates the concept of the lock-in wavenumber. Data displayed in figure 6(*b*) for small Pr values ($Pr < 0.08$) demonstrate coexistence of structures associated with the parametric resonance which are locked-in with the primary state, as well as structures unlocked from the primary state and dominated by the RB effect.

From the above global look on the flow responses, we select a few representative fluids ($Pr = 7$, 0.25, 0.08 and 0.04) to have a detailed look at. Figure 7 illustrates variations of Ra_{cr} and δ_{cr} as functions of α for Pr values selected to illustrate how system response changes as the strength of spatial modulations increases. Figure 7(*a*,*b*) provides data for the weakest modulation ($Pr = 7$). The smallest $Ra_{cr} = Ra_{min} = 2901.2$ is found for $\alpha = \alpha_{cr} = 3.93$. Modulation with larger α results in a rapid increase of Ra_{cr} with its variations following an asymptote $Ra_{cr} = 236\alpha^{1.5}$. In this limit a thermal boundary layer develops near the lower wall with the bulk of the fluid perceiving the edge of this boundary layer as a uniformly heated wall and the secondary state being driven by the classical RB instability – we shall refer to it as the RB limit (Hossain & Floryan 2013*b*). A decrease of α leads to a rapid increase of Ra_{cr} with no transition to a secondary state found for $\alpha < \alpha_{lb} = 3.6$. Variations of the critical wavenumber show that the forms of the primary and secondary states are locked-in as $2\delta_{cr} = \alpha$ when $\alpha < \alpha_{lc} = 4.37$, where α_{lc} stands for the lock-in wavenumber. One could appreciate that the tight lock-in of the primary state and the disturbance structures are responsible for the rapid stabilization at lower values of α after the minimum value of Ra_{cr} is reached. This lock-in is broken for large α with

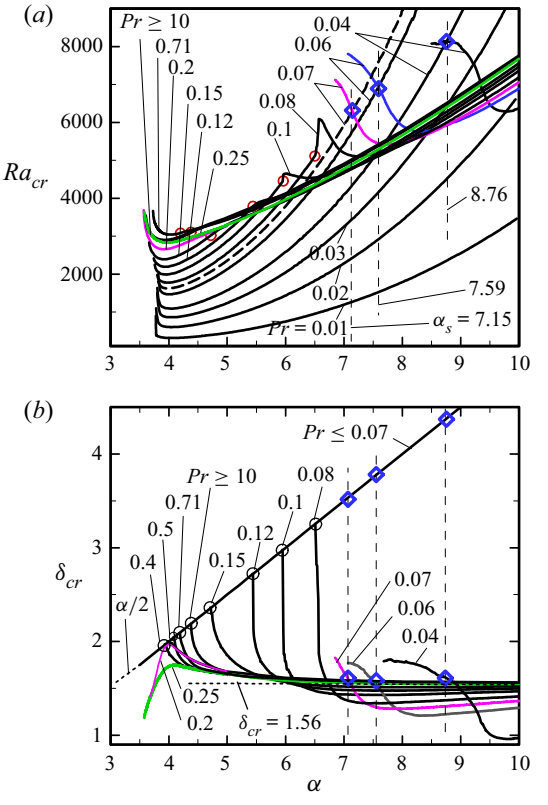

Figure 6. Variations of the critical Rayleigh number Ra_{cr} (*a*) and the critical disturbance wavenumber δ_{cr} (*b*) as functions of α. The lock-in points, which define the lock-in wavenumber α_{lc}, are marked with circles and points where two different disturbance structures co-exist are marked with diamonds. Data for $Pr = 0.4$, 0.5 and 0.71 overlap in plot (*a*).

$\delta_{cr} \to 1.56$ (the RB limit) from above as $\alpha \to \infty$. There is a transition zone between the locked-in and the large-α states which will be discussed later.

Reduction of Pr to 0.25 eliminates the lock-in effect as illustrated in figure 7(*c*,*d*). The large-α asymptotes for Ra_{cr} and δ_{cr} remain unchanged but δ_{cr} varies in a non-monotonic manner in the transition zone and approaches the RB limit from below. The minimum of $Ra_{cr} = Ra_{min} = 2826.8$ occurs at $\alpha_{min} = 3.97$ and the maximum of $\delta_{cr} = \delta_m = 1.74$ occurs at $\alpha_m = 4.19$.

Reduction of Pr to 0.08 brings back the lock-in as illustrated in figure 7(*e*,*f*). There are two distinct zones in the variations of Ra_{cr} separated by $\alpha_{lc} = 6.51$. In the left zone the primary and secondary states are locked-in with the minimum $Ra_{cr} = Ra_{min,1} = 1773.5$ occurring at $\alpha_{min,1} = 3.97$. The right zone is unlocked and has its own minimum of $Ra_{cr} = Ra_{min,2} = 5104.9$ occurring at $\alpha_{min,2} = 7.25$. The transition between both zones is complex – it begins, when moving from left to right, with a break of the lock-in at $\alpha_{lc} = 6.51$ followed by a rapid increase of Ra_{cr} up to $Ra_{cr} = 6090$ at $\alpha = 6.57$ and a rapid decrease of δ_{cr} from 3.25 down to 1.87. The growth of Ra_{cr} terminates at a cusp with Ra_{cr} decreasing to its local minimum and then approaching the RB asymptote with a further increase of α. At the same time the critical wavenumber approaches the RB limit from below. The parametric resonance dominates in the left zone while the RB effect dominates in the right zone.

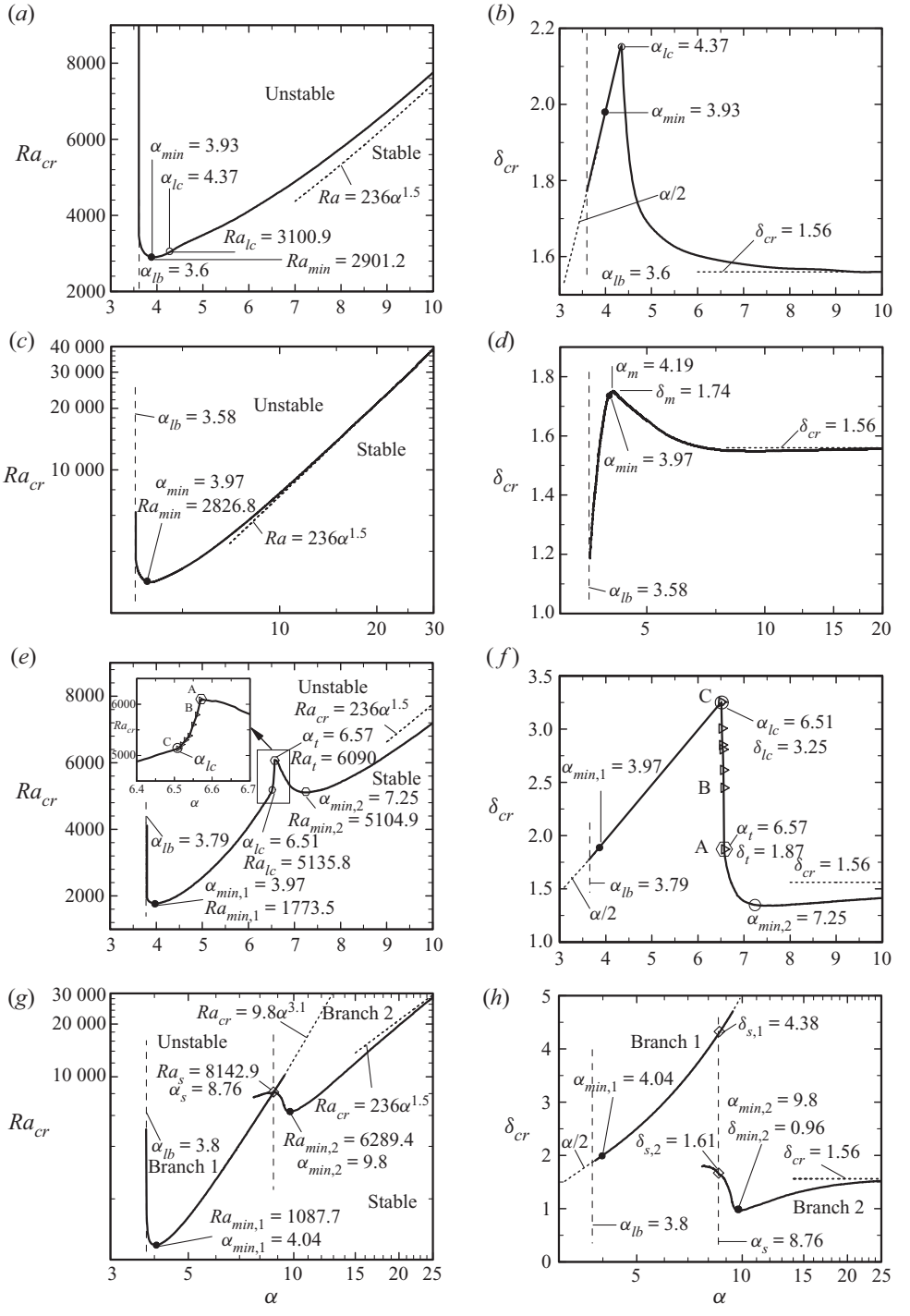

Figure 7. Variations of the critical Rayleigh number Ra_{cr} (*a*,*c*,*e*,*g*) and the critical disturbance wavenumber δ_{cr} (*b*,*d*,*f*,*h*) as functions of α. Plots (*a–h*) provide data for $Pr = 7$, 0.25, 0.08, 0.04.

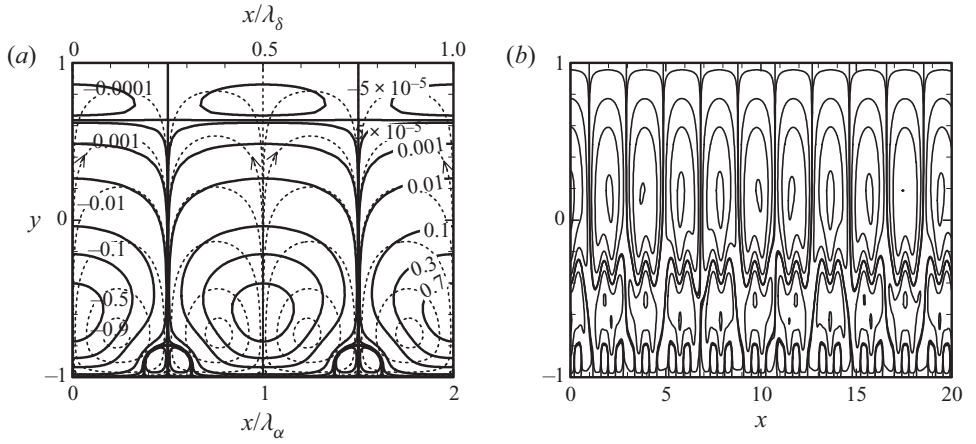

Figure 8. Disturbance flow field for branch 1 (*a*) and branch 2 (*b*) for conditions corresponding to the intersection of both branches ($\alpha = \alpha_s = 8.76$, $Ra_{cr} = Ra_s = 8142.9$) for $Pr = 0.04$. In plot (*a*) the primary and secondary flow fields are represented using dashed and solid lines, respectively. The primary and secondary flow streamfunctions have been normalized with their maxima. In plot (*b*) the contour lines correspond to $\psi_2(x, y)/\psi_{2,max} = 0, 0.01, 0.2, 0.5, 0.9$.

The final case corresponds to $Pr = 0.04$ (see figure 7*g*,*h*) and it demonstrates formation of two distinct branches of the critical curve corresponding to different secondary structures. The left branch has a minimum of $Ra_{cr} = Ra_{min,1} = 1087.7$ occurring at $\alpha_{min,1} = 4.04$ – this is the parametric resonance branch (with the lock-in; note that the α-axis has a log scale) and it has its own large-α asymptote. The right branch has a minimum $Ra_{cr} = Ra_{min,2} = 6289.4$ occurring at $\alpha_{min,2} = 9.8$ – this is the RB branch with its specific large-α asymptote. Both branches cross (intersect) at $(Ra_s, \alpha_s) = (8142.9, 8.76)$. The secondary structures for branch 1 at the intersection point are characterized by $\delta_{cr} = \delta_{s.1} = 4.38$ and, for branch 2, by $\delta_{cr} = \delta_{s,2} = 1.61$ – these two very distinct structures co-exist for the same heating conditions. The locked-in patterns (branch 1) at the onset of the instability are illustrated in figure 8(*a*) for conditions corresponding to the intersection of both branches, i.e. $\alpha_s = 8.76$. The sub-harmonic relation between the primary and secondary convection is clearly visible. The emergence of the second layer of rolls at the top of the slot is observed. The unlocked pattern occurring for the same conditions (branch 2), shown in figure 8(*b*), is markedly different and its form is difficult to characterize. One can further corroborate the existence of two branches for the case of $Pr = 0.04$ using figure 9 which depicts a set of neutral stability curves ($\sigma_i = 0$) for several Ra values in a $\alpha - \delta$ plane. Branch 1 extends from low-α to high-α zones whereas branch 2 exists at high α only. The susceptibility of the disturbances to form a locked-in pattern, and the interplay between the appearance of a conduction layer and the formation of a second layer of rolls (near the top wall) producing a stabilizing effect, play an important role for such a manifestation of unstable zones.

Further reduction of Pr preserves both branches but pushes the right branch towards larger values of α (details not shown). One can conclude that there are two instability mechanisms, one driven by the parametric resonance and the other by the RB effect with the lock-in wavenumber α_{lc} defining a border in-between, with the separation wavenumber α_s assuming this role when two stability branches are formed. Both instability mechanisms are at par for large Pr values but its reduction gives preference to the former one for $\alpha = 0(1)$ and pushes the latter one towards larger α values.

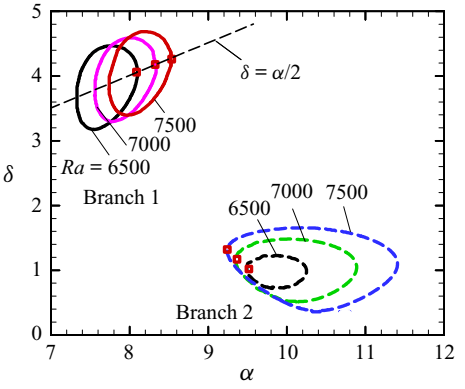

Figure 9. Variations of the neutral stability ($\sigma_i = 0$) conditions for a fixed Ra as a function of α and δ for $Pr = 0.04$. The inner area of each closed curve identifies the unstable zone. Square symbols denote the critical conditions (shown in figure 7*g*,*h*) at each Ra.

The character of fluid movement is dictated by the dispersion relation $\delta_{cr} = \delta_{cr}(\alpha)$ which has a simple form for $\alpha \to \infty$ as in this limit $\delta_{cr} \to 1.56$, and in the locked-in zones where $\delta_{cr} = \alpha/2$ – these cases represent simple commensurate states. To discuss possible states in the in-between zones, the need to introduce a measure of system periodicity Λ – it can be measured either in terms of the number N_δ of the disturbance wavelengths or in terms of the number N_α of the heating wavelengths, i.e. $\Lambda = N_\delta(2\pi/\delta) = N_\alpha(2\pi/\alpha)$. Both N_α and N_δ take (different) integer values; Λ can be either finite (commensurate periodic states) or infinite (incommensurate aperiodic states) depending if the ratio δ/α is rational (the former case) or irrational (the latter case). A small change of any of the wavenumbers may change Λ by orders of magnitude. It is simple to show that in the large-α limit there is a discrete band of α values being able to produce a particular N_δ and α corresponding to a specified N_δ given as $\alpha = 1.56N_\alpha/N_\delta$ which means that the secondary convection has features of a frustrated system (Nixon *et al.* 2013).

Flow in the in-between zone exhibits interesting features. Commensurate states have been identified by searching for the lowest common denominator of α and δ_{cr} and expressing their periodicity in terms of N_δ. These structures form bands in the (N_δ, α)-plane which are categorized by the value of N_δ for $\alpha \to \infty$ as shown in figure 10. These bands have been determined numerically and the identification of pairs (δ_{cr}, α) corresponding to a given band involved trial and error. A data set of (δ_{cr}, α) was determined using suitable step sizes $\Delta\alpha$ (e.g. 1/100, 1/12), computing δ_{cr} with four digits accuracy and retaining only two digits to be consistent with the large-α limit of $\delta_{cr} = 1.56$. This process does not provide access to all possible commensurate states but illustrates nevertheless the wealth of possible responses.

Figure 10 illustrates possible states using N_δ. There is just a single band in the lock-in zone, but many distinct bands in the transition zone with similar characteristics for all Pr values. These bands display certain inter-relations in the large-α limit, i.e. there are sets corresponding to a sequential doubling up of the system wavelength, i.e. $N_\delta = 39, 78, 156$ and $N_\delta = 117, 234, 468$, and then tripling up, i.e. $N_\delta = 39, 117$. Many other bands are possible, but their identification is compromised by the accuracy of the solution of the eigenvalue problem – while α is specified exactly, δ_{cr} is affected by the numerical error. The solution used spectral discretization, but computations relied on double

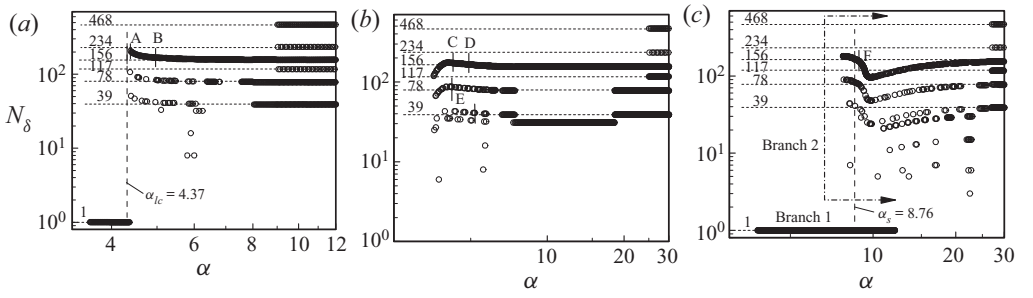

Figure 10. Variations of the wavelength of the flow system as a function of α at the onset measured in terms of the disturbance wavelengths N_δ. Plots (*a–c*) provide data for $Pr = 7, 0.25, 0.04$. Flow structures for points identified using letters (*a–f*) are displayed in figure 11.

precision arithmetic. The resolution can be improved by using quadruple precision or higher, but this was not possible in the present study.

Figure 11 provides data for characterization of flow patterns for $N_\delta = 156$ which are like those found for other N_δ values. The characterization is done using distributions of the v_2-velocity component along the mid-section of the slot at the onset and normalized with their maxima to focus on patterns only. Each cycle of v_2 signifies one pair of convection rolls. Figure 11(*a*,*f*) demonstrate the formation of 'beating' patterns for α slightly above the lock-in value for all Pr values – the secondary motion consists of nearly identical rolls whose strength varies periodically. Figure 11(*b–d*) demonstrate the formation of 'wavy' patterns for α further away from α_{lc}. Certain x-locations show a stronger upward movement while others show an opposite trend. A detailed look demonstrates roll pairs of different properties – at the beginning of a spatial cycle one roll is wider but with a less intense motion while the other is smaller with a more intense motion (see figure 12*a*) – their role is reversed after a half-cycle (figure 12*b*). The 'beating' pattern was not found for $Pr = 0.25$ (no locked-in states) but 'wavy' patterns exhibit an abrupt change of the amplitude envelop (figure 11*c*,*d*). A completely different pattern is shown in figure 11(*e*) with every other roll being much narrower and much stronger. Only 'beating' patterns were found for $Pr = 0.04$ (figure 11*f*). Analysis of the local wavenumber δ_{local} determined from the distance between two subsequent zeros of v_2 quantifies competition between the locked-in wavenumber $\delta_{cr} = \alpha/2$ and the RB wavenumber $\delta_{cr} = 1.56$, with the 'beating' pattern strongly influenced by the lock-in and producing wide and flat maxima separated by narrow minima giving the appearance of a solitary phase modulation and forming a lattice parallel to the rolls (details not given). Solitons are known to mediate transition between the commensurate and incommensurate patterns (Lowe & Gollub 1985; Mccoy *et al.* 2008). For the 'wavy' pattern, these two effects are at par resulting in a rapid periodic adjustment of δ_{local} with its minima corresponding to locations where clockwise and anti-clockwise rotations have a similar intensity while its maxima correspond to locations with a preferred direction of rotation (details not shown).

Different types of responses are summarized in figure 13(*a*). Type A occurs for large Pr and is characterized by a nearly constant lock-in wavenumber α_{lc} and the lock-in critical Rayleigh number Ra_{lc}. Type B does not involve the lock-in. Type C includes the lock-in with rapid variations of both α_{lc} and Ra_{lc}. Type D involves two separate branches so the concepts of α_{lc} and Ra_{lc} do not apply – one branch is associated with the lock-in and the other is unlocked. Variations of δ_{cr} as a function of Pr for selected α values displayed in figure 13(*b*) illustrate peculiarity of the system response to variations of Pr, as there is a

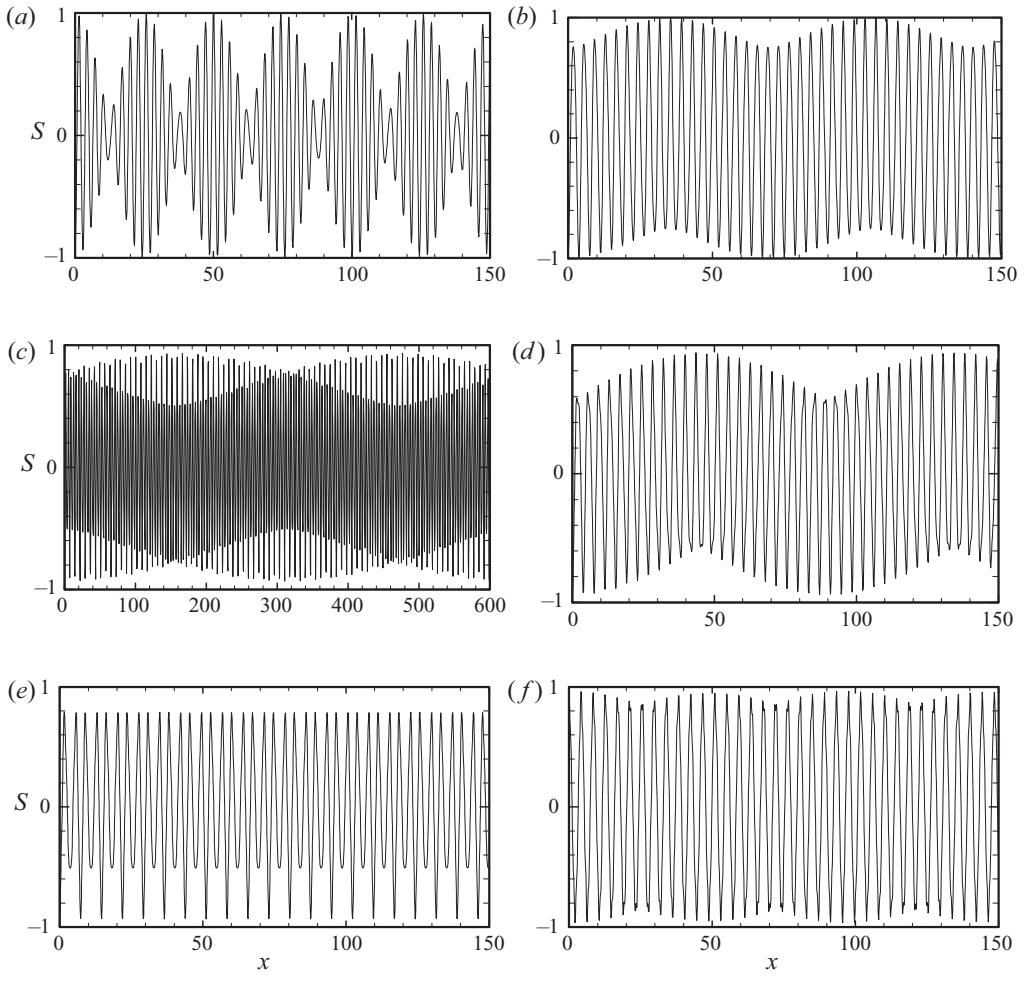

Figure 11. Variations of $S = v_2(x, 0)$ normalized with its maximum at $y = 0$ for $N_\delta = 156$ (except plot (*e*) where $N_\delta = 78$) and selected Pr values. The onset conditions in plots (*a–f*) are $(\alpha, \delta_{cr}, Ra_{cr}) = (4.39, 2.07, 3116.8)$, $(4.95, 1.68, 3454.1)$, $(4.31, 1.72, 2939.3)$, $(4.91, 1.66, 3244.2)$, $(4.3, 1.72, 2934.8)$, $(9.01, 1.48, 7961.4)$ and the corresponding points are marked in figure 10 using letters identifying subfigures. Results are shown for (*a*) $Pr = 7$, (*b*) $Pr = 7$, (*c*) $Pr = 0.25$, (*d*) $Pr = 0.25$, (*e*) $Pr = 0.25$, (*f*) $Pr = 0.04$.

range of α where both small enough and large enough Pr values produce locked-in states while the in-between Pr values do not show the lock-in – this zone corresponds to a type B response identified in figure 13(*a*).

In order to determine the lowest heating intensity required to induce secondary convection assuming that one has an option to choose the type of fluid and the heating wavenumber, we construct figure 14 which depicts the required minimum Rayleigh number $Ra_{cr,min}$ for each heating wavenumber denoted by α_{min} and the critical disturbance wavenumber by $\delta_{cr,min}$ as functions of Pr. The responses can also be qualitatively categorized as type A,B,C and D as the border lines shown in figure 14 correspond (qualitatively) to the borders identified in figure 13(*a*). In type A (fluids with $Pr > 0.4$), intense heating is required (the $Ra_{cr,min}$ is higher) to induce the secondary convection, the heating wavenumber α_{min} monotonically decreases from 4.05 to an asymptotic value of 3.93, and α_{min} and $\delta_{cr,min}$ are locked-in. In type B, which occurs for Pr between ~ 0.4

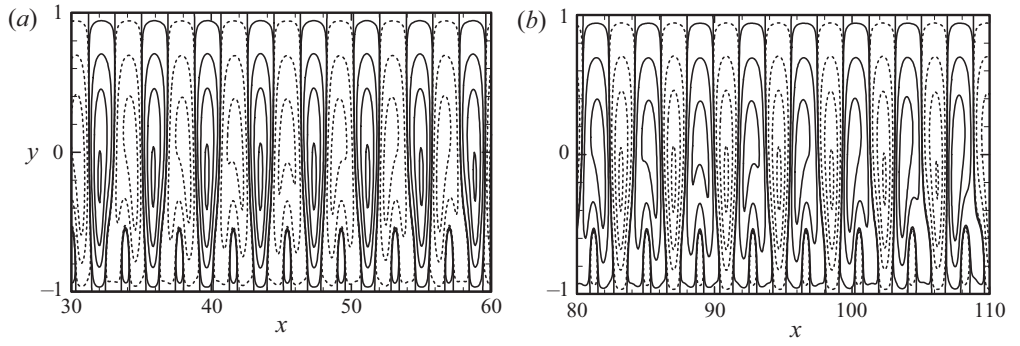

Figure 12. The disturbance flow field corresponding to the 'wavy' pattern at the critical point $(\alpha, \delta_{cr}, Ra_{cr}) = (4.91,\ 3244.2,\ 1.66)$ for $Pr = 0.25$. The contour lines shown correspond to $\psi_2(x, y)/\psi_{2,max} = 0, 0.01, 0.1, 0.5, 0.9$. Solid and dotted lines are used to identify rolls rotating in the opposite directions. This pattern belongs to the wavelength band $N_\delta = 156$.

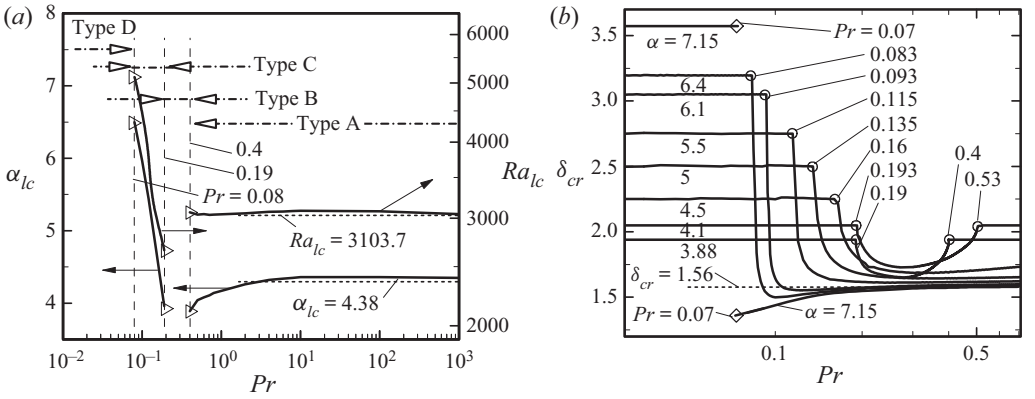

Figure 13. (*a*) Variations of the lock-in conditions, i.e. the lock-in heating wavenumber α_{lc} and the critical Rayleigh number at the lock-in point Ra_{lc}, as functions of Pr. Triangles identify ends of the lock-in intervals. (*b*) Variations of the critical wavenumber δ_{cr} as a function of Pr for selected α values. Diamonds identify conditions where locked-in and unlocked structures co-exist. Circles denote ends of the lock-in intervals. The RB limit of $\delta_{cr} = 1.56$ is marked using a thin dotted line.

and ~ 0.19, intensity of the required heating and α_{min} gradually decrease with a decrease of Pr, and the lock-in does not occur. In type C, which occurs for $\sim 0.08 < Pr <\sim 0.19$, intensity of the required heating rapidly decreases with a decrease of Pr, α_{min} and $\delta_{cr,min}$ become locked-in with both wavenumbers slightly increasing with a decrease of Pr. In type D, which occurs for fluids with $Pr < 0.04$, weak heating (e.g. as low as $Ra_{cr,min} = 314.3$ for $Pr = 0.01$) is sufficient to induce the secondary convection, the lock-in occurs and both α_{min} and $\delta_{cr,min}$ remain nearly constant at 4.02 and 2.01, respectively.

4. Summary

Multiple forms of response of a fluid layer exposed to spatially periodic heating were identified. The system is charaterized by two wavenumbers: one characterizes the pattern of externally imposed heating (α), while the other is determined by the instability processes (δ). The system response is driven by a competition between two instability mechanisms, i.e. the spatial parametric resonance and the RB mechanism. The spatial

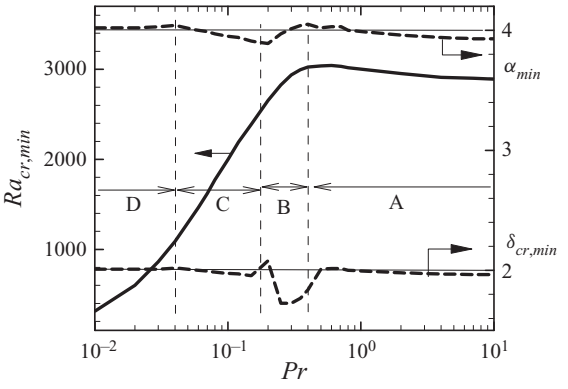

Figure 14. Variations of the minimum Rayleigh number $Ra_{cr,min}$ (solid line) required to induce secondary convection, the corresponding heating wavenumber α_{min} (upper dashed line) and the critical disturbance wavenumber $\delta_{cr,min}$ (lower dashed line) as functions of Pr.

parametric-resonance-dominated response exhibits the characteristic lock-in between the primary and secondary convection. Both states are unlocked when the RB instability dominates, and the structure of the resulting convection is very similar to RB convection. Convection in the transition zone between the lock-in states and the RB-like states creates a spectrum of commensurate and incommensurate states with only the former being accessible to numerical solutions due to limitations of computer accuracy. These states can be organized into discrete bands of wavelengths with the resulting movement exhibiting 'wavy' and 'beating' patterns. Since the bands reported in this paper are constructed by retaining two digits from a four-digits-accurate computed δ_{cr}, other patterns may emerge if the bands are constructed using more accurate data.

The first mechanism referred to above, i.e. spatial parametric resonance, dominates if the spatial modulation of the primary state is sufficiently strong while the second one, the RB instability, dominates for weak spatial modulations. The strength of modulation decreases with an increase of Pr and an increase of α. An increase of Ra increases the intensity of the fluid motion but it increases modulation only for $\alpha <\sim 10$ and has no effect on the modulation for $\alpha > 10$. The possible responses for different fluids can be divided into four types. In type A, which occurs for fluids with $Pr >\sim 0.4$, the spatial parametric resonance dominates for $\alpha < 4.5$ resulting in a lock-in of the critical wavenumber δ_{cr} with the heating wavenumber by a sub-harmonic relation, e.g. $\delta_{cr} = \alpha/2$. For larger values of α (e.g. $\alpha > 10$), a convection boundary layer forms near the heated wall producing a uniform vertical temperature gradient above it leading to the dominance of the RB mechanism and elimination of any relation between the primary and secondary flow patterns. In the in-between zone of α, where neither mechanism dominates, an interplay of both mechanisms creates conditions where a small change in α results in a major change in the flow pattern, thereby providing a wealth of possible system responses. Morphing between different convection patterns may occur in response to minor changes of the heating pattern. In type B, which occurs for Pr between $\sim$0.4 and $\sim$0.19, the RB mechanism dominates and the lock-in between the instability and the heating patterns does not occur. In type C, which occurs for $\sim 0.08 < Pr <\sim 0.19$, the stronger spatial modulation causes a pattern of instability to lock-in with the heating pattern for α values up to $\alpha = \sim 7$. The RB effect prevails for $\alpha > 10$, and in the in-between zone of α ($\alpha = 7 \sim 10$) a wealth of possible patterns occurs, similarly as in type A. It is found that for type C, the change of the

lock-in wavenumber α_{lc} and the change of the lock-in Rayleigh number Ra_{lc} occur rapidly with the change of Pr, whereas for type A, the changes of α_{lc} and Ra_{lc} are very gradual (α_{lc} vs Pr and Ra_{lc} vs Pr curves are almost flat). In type D, which occurs for $Pr < 0.08$, two separate critical instability branches have been identified. Branch 1 describes the critical conditions for parametric resonance and corresponds to disturbances whose structure is locked-in with the heating pattern. Branch 2 describes the critical conditions for the RB-dominated instability and corresponds to disturbances whose patterns have no relation with the heating patterns. The critical conditions when both types of patterns co-exist have been identified. Among the four types of responses outlined above, it is observed that the locked-in pattern (branch 1) of type D requires the weakest heating (e.g. as low as $Ra_{cr,min} = 314.3$ for $Pr = 0.01$ at $\alpha = 4.02$) to create secondary motions.

Similar responses are expected to occur when heating is applied to the upper wall. Heating of both walls introduces a phase difference that may qualitatively change the system response. The addition of weak forced convection is not expected to produce major changes.

Funding. This work has been carried out with the support from NSERC of Canada.

Declaration of interests. The authors report no conflict of interest.

Author ORCIDs.
M.Z. Hossain https://orcid.org/0000-0001-6484-4905;
J.M. Floryan https://orcid.org/0000-0003-3296-4122.

Appendix A. Primary convection formulation: method of solution

This appendix illustrates the method of solution of the governing equations (2.4) describing the primary convection presented in § 2.

We start the solution of the governing equations (2.4) by introducing the streamfunction $\psi_1(x, y)$ defined in the usual manner as $u_1 = \partial\psi_1/\partial y$, $v_1 = -\partial\psi_1/\partial x$, and eliminating the pressure field from the momentum equations resulting in

$$\nabla^4\psi_1 - Ra\frac{\partial\theta_1}{\partial x} - RaPr^{-1}\frac{\partial\theta_c}{\partial x} = N_1, \tag{A1a}$$

$$\nabla^2\theta_1 = N_2, \tag{A1b}$$

where terms involving products and nonlinearities are expressed as

$$N_1 = \frac{\partial}{\partial y}\left(\frac{\partial}{\partial x}\langle u_1u_1\rangle + \frac{\partial}{\partial y}\langle u_1v_1\rangle\right) - \frac{\partial}{\partial x}\left(\frac{\partial}{\partial x}\langle u_1v_1\rangle + \frac{\partial}{\partial y}\langle v_1v_1\rangle\right), \tag{A2}$$

$$N_2 = Pr\left(\frac{\partial}{\partial x}\langle u_1\theta_1\rangle + \frac{\partial}{\partial y}\langle v_1\theta_1\rangle\right) + \frac{\partial}{\partial x}\langle u_1\theta_c\rangle + \frac{\partial}{\partial y}\langle v_1\theta_c\rangle. \tag{A3}$$

We assume the solution in the form of Fourier expansions,

$$[\psi_1, \theta_1](x, y) = \sum_{n=-\infty}^{n=+\infty}[\varphi_1^{(n)}, \phi_1^{(n)}]e^{in\alpha x}, \tag{A4a}$$

$$[u_1, v_1](x, y) = \sum_{n=-\infty}^{n=+\infty}[u_1^{(n)}, v_1^{(n)}]e^{in\alpha x}, \tag{A4b}$$

where $\varphi_1^n = \varphi_1^{(-n)*}$, $\phi_1^n = \phi_1^{(-n)*}$, $u_1^n = u_1^{(-n)*}$ and $v_1^n = v_1^{(-n)*}$ represent the reality conditions and stars denote complex conjugates, $u^{(n)} = D\varphi_1^{(n)}$, $v^{(n)} = \mathrm{i}\,n\alpha\varphi_1^{(n)}$ and $D = \partial/\partial y$. The nonlinear and product terms are also expressed in terms of Fourier expansions in the form

$$[\langle u_1u_1\rangle, \langle u_1v_1\rangle, \langle v_1v_1\rangle](x,y) = \sum_{n=-\infty}^{n=+\infty} [\langle u_1u_1\rangle^{(n)}, \langle u_1v_1\rangle^{(n)}, \langle v_1v_1\rangle^{(n)}]\mathrm{e}^{\mathrm{i}n\alpha x}, \tag{A4c}$$

$$[\langle u_1\theta_1\rangle, \langle v_1\theta_1\rangle, \langle u_1\theta_c\rangle, \langle v_1\theta_c\rangle](x,y) = \sum_{n=-\infty}^{n=+\infty} [\langle u_1\theta_1\rangle^{(n)}, \langle v_1\theta_1\rangle^{(n)}, \langle u_1\theta_c\rangle^{(n)}, \langle v_1\theta_c\rangle^{(n)}]\mathrm{e}^{\mathrm{i}n\alpha x}. \tag{A4d}$$

Substitution of (A4) into (A1) and separation of Fourier components results in the following system of ordinary differential equations for the modal functions:

$$D_n^2{\varphi_1}^{(n)} - \mathrm{i}\,n\alpha Ra\phi_1^{(n)} = \mathrm{i}\,n\alpha Ra\theta_c^{(n)} + N_1^{(n)}, \tag{A5a}$$

$$D_n{\phi_1}^{(n)} = N_2^{(n)}. \tag{A5b}$$

Here $D = \mathrm{d}/\mathrm{d}y$, $D^2 = \mathrm{d}^2/\mathrm{d}y^2$, $D_n = D^2 - n^2\alpha^2$, $D_n^2 = D_n(D_n)$, $N_1^{(n)} = \mathrm{i}\,n\alpha D\langle u_1u_1\rangle^{(n)} + D^2\langle u_1v_1\rangle^{(n)} + \mathrm{i}\,n^2\alpha^2\langle u_1v_1\rangle^{(n)} - \mathrm{i}\,n\alpha D\langle v_1v_1\rangle^{(n)}$, $N_2^{(n)} = Pr(\mathrm{i}\,n\alpha\langle u_1\theta_1\rangle^{(n)} + D\langle v_1\theta_1\rangle^{(n)}) + \mathrm{i}\,n\alpha\langle u_1\theta_c\rangle^{(n)} + D\langle v_1\theta_c\rangle^{(n)}$. The required boundary conditions have the form

$${\varphi_1}^{(n)}(\pm1) = 0, D{\varphi_1}^{(n)}(\pm1) = 0, {\phi_1}^{(n)}(\pm1) = 0 \quad \text{for} -\infty < n < +\infty. \tag{A5c–e}$$

In the system (A5) the unknown linear terms have been placed on the left-hand side, and the nonlinear and product terms have been placed on the right-hand side. For the purpose of numerical solution, expansions (A4) have been truncated after N_M Fourier modes. The discretization method uses the Chebyshev collocation technique based on the Gauss–Chebyshev–Lobatto points (Canuto *et al.* 1996). The resulting nonlinear algebraic system was solved using an iterative technique combined with under-relaxation.

Appendix B. Secondary convection formulation: method of solution

This appendix illustrates the solution procedure of the governing equations describing the secondary convection presented in § 3.

Similar to the primary convection, we introduce the disturbance streamfunction $\psi_2(x,y)$ defined as $u_2 = \partial\psi_2/\partial y$, $v_2 = -\partial\psi_2/\partial x$, and eliminate the pressure field p_2 from the disturbance momentum equations.

The forms of disturbances described by (3.3)–(3.4) are applied to ψ_2 and θ_2 as

$$[\boldsymbol{\psi_2}, \theta_2](x,y,t) = \sum_{m=-\infty}^{m=+\infty} [\boldsymbol{\Psi_2^{(m)}}, \Theta_2^{(m)}](y)\mathrm{e}^{\mathrm{i}\,m\alpha x}\mathrm{e}^{\mathrm{i}(\delta x - \sigma t)} + \text{c.c.} \tag{B1}$$

Substitution of (B1) into the disturbance equations (3.2) and separation of Fourier components result, after a rather tedious algebra, in a system of linear homogeneous

ordinary differential equations in the form

$$A^{(m)}\Psi_2^{(m)} - \mathrm{i}\,t_m Ra\Theta_2^{(m)} = \mathrm{i}\sum_{n=-\infty}^{n=+\infty}[t_n D\varphi_1^{(m-n)}H^{(n)}\Psi_2^{(n)} + (m-n)\alpha I^{(m-n)}\varphi_1^{(m-n)}D\Psi_2^{(n)} - (m-n)\alpha\varphi_1^{(m-n)}H^{(n)}D\Psi_2^{(m)} - t_n I^{(m-n)}D\varphi_1^{(m-n)}\Psi_2^{(n)}], \tag{B2a}$$

$$C^{(m)}\Theta_2^{(m)} = \mathrm{i}\,Pr\sum_{n=-\infty}^{n=+\infty}[t_n D\varphi_1^{(m-n)}\Theta_2^{(n)} + (m-n)\alpha\vartheta_1^{(m-n)}D\Psi_2^{(n)} - (m-n)\alpha\varphi_1^{(m-n)}D\Theta_2^{(m)} - t_n D\vartheta_1^{(m-n)}\Psi_2^{(n)}], \tag{B2b}$$

where

$$\left.\begin{aligned} A^{(m)} &= (D^2 - t_m^2)^2 + \mathrm{i}\,\sigma(D^2 - t_m^2),\\ C^{(m)} &= D^2 - t_m^2 + \mathrm{i}\,Pr\sigma,\\ \vartheta_1^{(m)} &= Pr^{-1}\theta_c^{(m)} + \phi_1^{(m)},\\ I^{(m-n)} &= D^2 - (m-n)^2\alpha^2,\\ H^{(n)} &= D^2 - t_n^2,\\ t_m &= \delta + m\alpha,\\ t_n &= \delta + n\alpha. \end{aligned}\right\} \tag{B2c}$$

The boundary conditions take the form

$$\Psi_2^{(m)}(\pm1) = 0, \quad D\Psi_2^{(m)}(\pm1) = 0, \quad \Theta_2^{(m)}(\pm1) = 0 \quad \text{for } -\infty < m < +\infty. \tag{B2d–f}$$

Equations (B2) are truncated after N_M modes and are discretized with spectral accuracy using the Chebyshev collocation method with N_T collocation points (Canuto *et al.* 1996). The resulting eigenvalue problem is solved by the 'inverse iteration' technique as described in Saad (2011).

References

Bénard, H. 1900 Les tourbillons cellulaires dans une nappe liquide. *Rev. Gén. Sci. Pure Appl.* **11**, 1261–1271.

Bloch, F. 1928 Über die quantenmechanik der elektronen in kristallgittern. *Z. Phys.* **52**, 555–600.

Bodenschatz, E., Pesch, W. & Ahlers, G. 2000 Recent developments in Rayleigh–Bénard convection. *Annu. Rev. Fluid Mech.* **32**, 709–778.

Canuto, C., Hussaini, M.Y., Quarteroni, A. & Zang, T.A. 1996 *Spectral Methods*. Springer.

Chandrasekhar, S. 1961 *Hydrodynamic and Hydromagnetic Stability*. Dover.

Floryan, J.M. 1997 Stability of wall bounded shear layers with simulated distributed surface roughness. *J. Fluid Mech.* **335**, 29–55.

Floryan, J.M. & Inasawa, A. 2021 Pattern interaction effect. *Sci. Rep.* **11**, 14573.

Freund, G., Pesch, W. & Zimmermann, W. 2011 Rayleigh–Bénard convection in the presence of spatial temperature modulations. *J. Fluid Mech.* **673**, 318–348.

Hossain, M.Z. & Floryan, J.M. 2013*a* Heat transfer due to natural convection in a periodically heated slot. *Trans. ASME J. Heat Transfer* **135**, 022503.

Hossain, M.Z. & Floryan, J.M. 2013*b* Instabilities of natural convection in a periodically heated layer. *J. Fluid Mech.* **733**, 33–67.

Hossain, M.Z. & Floryan, J.M. 2014 Natural convection in a fluid layer periodically heated from above. *Phys. Rev.* E **90**, 023015.

HOSSAIN, M.Z. & FLORYAN, J.M. 2015 Natural convection in a horizontal fluid layer periodically heated from above and below. *Phys. Rev.* E **92**, 023015.

KELLY, R.E. & PAL, D. 1978 Thermal convection with spatially periodic boundary conditions: resonant wavelength excitation. *J. Fluid Mech.* **86**, 433–456.

KOSCHMIEDER, E.L. 1993 *Bénard Cells and Taylor Vortices*. Cambridge University Press.

KRISHNAN, M., UGAZ, V.M. & BURNS, M.A. 2002 PCR in a Rayleigh–Bénard convection cell. *Science* **298**, 793–793.

LOWE, M. & GOLLUB, J.P. 1985 Solitons and the commensurate–incommensurate transition in a convective nematic fluid. *Phys. Rev.* A **31**, 3893–3897.

LYUBIMOV, T.P., LYUBIMOV, D.V., MOROZOV, V.A., SCURIDIN, R.V., HADID, H.B. & HENRY, D. 2009 Stability of convection in a horizontal channel subjected to a longitudinal temperature gradient. Part 1. Effect of aspect ratio and Prandtl number. *J. Fluid Mech.* **635**, 275–295.

MANOR, A., HAGBERG, A. & MERON, E. 2008 Wavenumber locking in spatially forced patternforming systems. *Europhys. Lett.* **83**, 10005.

MANOR, A., HAGBERG, A. & MERON, E. 2009 Wavenumber locking and pattern formation in spatially forced systems. *New J. Phys.* **11**, 063016.

MCCOY, J.H., BRUNNER, W., PESCH, W. & BODENSCHATZ, E. 2008 Self-organization of topological defects due to applied constraints. *Phys. Rev. Lett.* **101**, 254102.

NIXON, M., RONEN, E., FRIESEM, A. & DAVIDSON, N. 2013 Observing geometric frustration with thousands of coupled lasers. *Phys. Rev. Lett.* **110**, 184102.

RAYLEIGH, LORD 1916 On convection currents in a horizontal layer of fluid, when the higher temperature is on the under side. *Phil. Mag.* **32**, 529–546.

SAAD, Y. 2011 *Numerical Methods for Large Eigenvalue Problems*, 2nd edn. SIAM.

VERZICCO, R. & CAMUSSI, R. 1999 Prandtl number effects in convective turbulence. *J. Fluid Mech.* **383**, 55–73.